



# A sustainable technique to solve growing energy demand: porous carbon nanoparticles as electrode materials for high-performance supercapacitors

Vinay S. Bhat<sup>1,2</sup> · Gurumurthy Hegde<sup>1</sup> · Mahmoud Nasrollahzadeh<sup>3</sup>

Received: 20 May 2020 / Accepted: 1 September 2020 / Published online: 12 September 2020  
© Springer Nature B.V. 2020

## Abstract

The present study demonstrates a facile, one-step pyrolysis method to synthesize porous carbon nanoparticles using widely distributed *Mimosa pudica* (Touch-me-not) biomass leaves at different temperatures. Multiple characterization techniques ( $N_2$  adsorption–desorption experiments, FESEM, XRD, Raman spectroscopy, XPS) demonstrate the morphological nature and excellent surface properties, with the surface area up to  $440.7 \text{ m}^2 \text{ g}^{-1}$ . The electrochemical studies of as-synthesized porous carbon nanoparticles, as electrodes, were carried out in both three and two electrode setups. The maximum specific capacitance obtained was  $356.1 \text{ F g}^{-1}$  at  $0.1 \text{ A g}^{-1}$  in  $4.0 \text{ M KOH}$  electrolyte. The symmetric supercapacitor showed a specific capacitance of  $126.8 \text{ F g}^{-1}$  at  $0.1 \text{ A g}^{-1}$  and a high energy density of  $34.5 \text{ Wh kg}^{-1}$ . The device also showed impeccable stability for 10,000 galvanostatic charge–discharge cycles with 99.2% Coulombic efficiency and capacitance retention of 81.39%. The stability of the device was investigated by floating method (aging), which showed 86.8% capacitance retention, suggesting a huge capacity of biomass-derived carbon materials for efficient and stable high-performance electrodes in electrochemical energy storage applications using an environmental-friendly approach. This study illustrates a sustainable approach to produce porous carbon nanoparticles for effective energy storage devices.

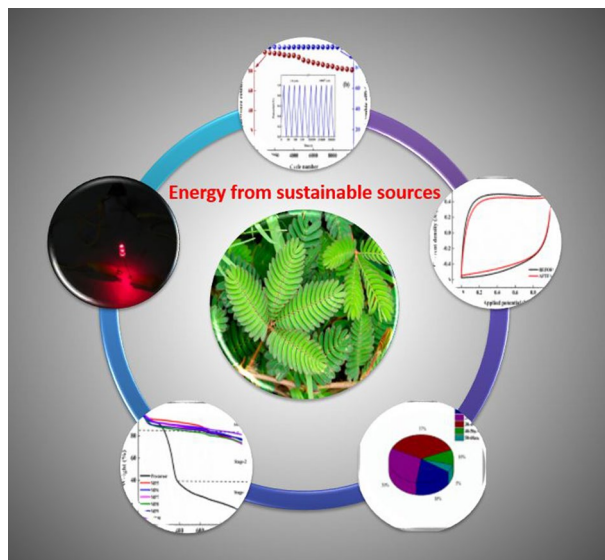
---

**Electronic supplementary material** The online version of this article (<https://doi.org/10.1007/s10800-020-01479-0>) contains supplementary material, which is available to authorized users.

---

Extended author information available on the last page of the article

## Graphic abstract



**Keywords** Touch-me-not · Porous carbon nanoparticles · Supercapacitors · High energy density

## 1 Introduction

Fossil fuel depletion and environmental pollution have promoted the growth of alternative energy technologies such as electrochemical energy systems, which encompass batteries, fuel cells, and electrochemical capacitors. These are capable of converting and storing energy from other modes, all in a small portable device [1]. Batteries and fuel cells exploit the energy stored in chemical bonds while supercapacitors store energy by the electrostatic separation between the electrolyte ions and electrode surface. Lithium-ion batteries (LIBs) suffer from recyclability and performance deterioration issues over long cycles. Supercapacitors have gained attention as promising green energy storage devices owing to their higher power density and long cycle stability than LIBs [2].

Electrochemical capacitors or supercapacitors are special types of capacitors, which have electrodes with very high surface area materials utilizing porous carbons or metal oxides [3]. The stored energy in supercapacitors is proportional to the capacitances of the electrodes. Capacitance in an electrode is dependent on three factors, as indicated in Eq. 1 [4].

$$C = \frac{\epsilon A}{d}, \quad (1)$$

where  $A$  is the surface area available to the electrolyte ions,  $d$  is the small separation between the electrode surface and electrolyte ions, and  $\epsilon$  is the electrolyte dielectric constant. The large energy storage potential of the supercapacitors compared

with conventional capacitors is mainly due to the small separation distance ( $\sim 1$  nm) between the electrode surface and electrolyte ions. Since capacitance and electrochemically active surface area are directly proportional, electrode materials with high porosity and the surface area result in larger electrochemically active surface area, thereby enhancing the capacitance. [5, 6]. Micropores with pore diameters of less than 2 nm, contribute towards a higher surface area. These micropores along with mesopores (pore diameters between 2 and 50 nm), are ideal for supercapacitor electrodes [4].

A major obstacle to supercapacitors is the insufficient energy density compared with batteries, which limits their applicability. Significant works have been carried out to increase the applicability of supercapacitors [7–13]. Energy density can be increased by developing electrode materials with high capacitance and electrolytes with wider potential windows. Although organic electrolytes and ionic liquids (ILs) can offer a wider potential window, they usually suffer from lower ionic conductivity. Aqueous electrolytes, which are inexpensive and easily handled, greatly simplify the fabrication and assembly processes of supercapacitors. Organic electrolytes and ILs, on the other hand, generally need purification under a controlled atmosphere to avoid moisture contamination. For acid and alkaline electrolytes, the cell voltages are generally limited to 1.0 V. However, in the present study, the synthesized novel porous carbon nanoparticles derived from the *Touch-me-not* plant allow the alkaline KOH electrolyte to be operated up to 1.4 V without decomposition of water and  $H_2/O_2$  gas evolution. The interaction between the electrode and electrolyte

has a profound influence on the supercapacitor performance. The plant is abundantly found and its leaf is well known for its nyctinastic movement. The electrode from the novel carbon material exhibited a very high specific capacitance of  $356.1 \text{ F g}^{-1}$  and the symmetric supercapacitor device, showed a high energy density of  $34.5 \text{ Wh kg}^{-1}$ , which places the synthesized materials among the best porous carbons in comparison with previously reported supercapacitors.

## 2 Materials and methods

### 2.1 Materials

The biomass precursor was collected from Sirsi, Karnataka, India. All the reagents/chemicals were of analytical grade and used as supplied to carry out the electrochemical measurements. Millipore water was utilized to prepare all the electrolyte solutions.

### 2.2 Preparation of carbon nanoparticles

Touch-me-not plant leaves were separated from rest of the plant. The leaves were dried in a vacuum oven at  $100 \text{ }^\circ\text{C}$  for 2 days. The dried leaves were ground and sieved in a  $60 \text{ }\mu\text{m}$  mesh in a vibratory sieve shaker (Aimil). The sieved powder was pyrolyzed under  $\text{N}_2$  atmosphere in a quartz tube furnace (NoPo Nanotechnologies) at different pyrolysis temperatures of  $500 \text{ }^\circ\text{C}$  to  $1000 \text{ }^\circ\text{C}$  at heating and cooling rates of  $10$  and  $2 \text{ }^\circ\text{C min}^{-1}$ , respectively. The residues obtained after pyrolysis were carbon nanoparticles and were labelled as MP5, MP6, MP7, MP8, MP9 and MP10, each representing the temperature ( $500, 600, 700, 800, 900,$  and  $1000 \text{ }^\circ\text{C}$ ) at which it was prepared. A detailed study on the synthesis of porous carbon nanoparticles has been previously reported by our group [14–17].

### 2.3 Characterization

Thermogravimetric analysis (TGA) was done on the raw and synthesized samples to study the thermal behaviour of the materials. Scanning electron microscopy (SEM) and energy dispersive spectroscopy (EDS) were performed to investigate the morphology and elemental composition of the material. Fourier transform infrared spectroscopy (FTIR) was carried out to analyse the functional groups present in the material. X-ray diffraction (XRD) was carried out to identify the crystallinity and phases. Raman spectroscopy was performed to identify the vibrational modes, defects, and graphitic nature of the materials. BET specific surface area and porosity were determined by  $\text{N}_2$  adsorption–desorption experiments.

## 2.4 Electrode preparation and electrochemical measurements

Electrochemical measurements were carried out using an AUTOLAB M204 instrument equipped with a frequency response analyser. Carbon nanoparticles, polyvinylidene difluoride (PVDF) and carbon black were mixed homogeneously in *N*-methyl pyrrolidone (NMP) as the solvent in 9:1:1 ratio, respectively. The mixture was coated onto nickel foam on  $1 \times 1 \text{ cm}^2$  area.  $4.0 \text{ M KOH}$  was used throughout the measurements as the electrolyte. A Pt wire was used as the counter electrode and saturated calomel electrode was used as reference electrode. A symmetric supercapacitor was fabricated using a Whatman glass fibre filter paper as separator and Ni substrate in  $4.0 \text{ M KOH}$  electrolyte.

## 3 Results and discussions

### 3.1 Thermal behaviour

The purity and composition of nanomaterials are very important before they are used for applications. The copious amount of the nanomaterial was heated and its behaviour was analysed from TGA. The percentage mass loss with temperature in the inert atmosphere is depicted in Fig. 1a. The samples were heated from  $25$  to  $1000 \text{ }^\circ\text{C}$  at  $10 \text{ }^\circ\text{C min}^{-1}$  heating rate. The precursor biomass sample mainly contains cellulose, hemicellulose and lignin. The initial mass loss around  $100 \text{ }^\circ\text{C}$  is due to the removal of moisture. Stage 2 represents a major weight loss. Pyrolysis of hemicellulose starts around  $200 \text{ }^\circ\text{C}$  while that of cellulose begins around  $300 \text{ }^\circ\text{C}$ . Hemicellulose is more amorphous with less strength. However, cellulose is more crystalline with long glucose monomer units and is pyrolyzed at higher temperatures than hemicellulose. Lignin, on the other hand, is more cross-linked, making it thermally stable [18]. Stage 3 represents the degradation of lignin with low or gradual mass loss. TGA was also carried out for carbon nanoparticles pyrolyzed at different temperatures. All the materials show remarkable thermal stability, with MP10 exhibiting the best thermal stability with very low decomposition and mass loss.

### 3.2 Morphology and porosity

The FESEM morphology of all the prepared carbon samples is depicted in Fig. S1. Since MP10 showed better behaviour in all the cases, here we represent the nano characterization data for MP10 and rest of the data is given in ESI. Figure 1b shows FESEM morphology of MP10. The morphology confirms the thermal decomposition of *Touch-me-not* leaves producing carbon with nano sized

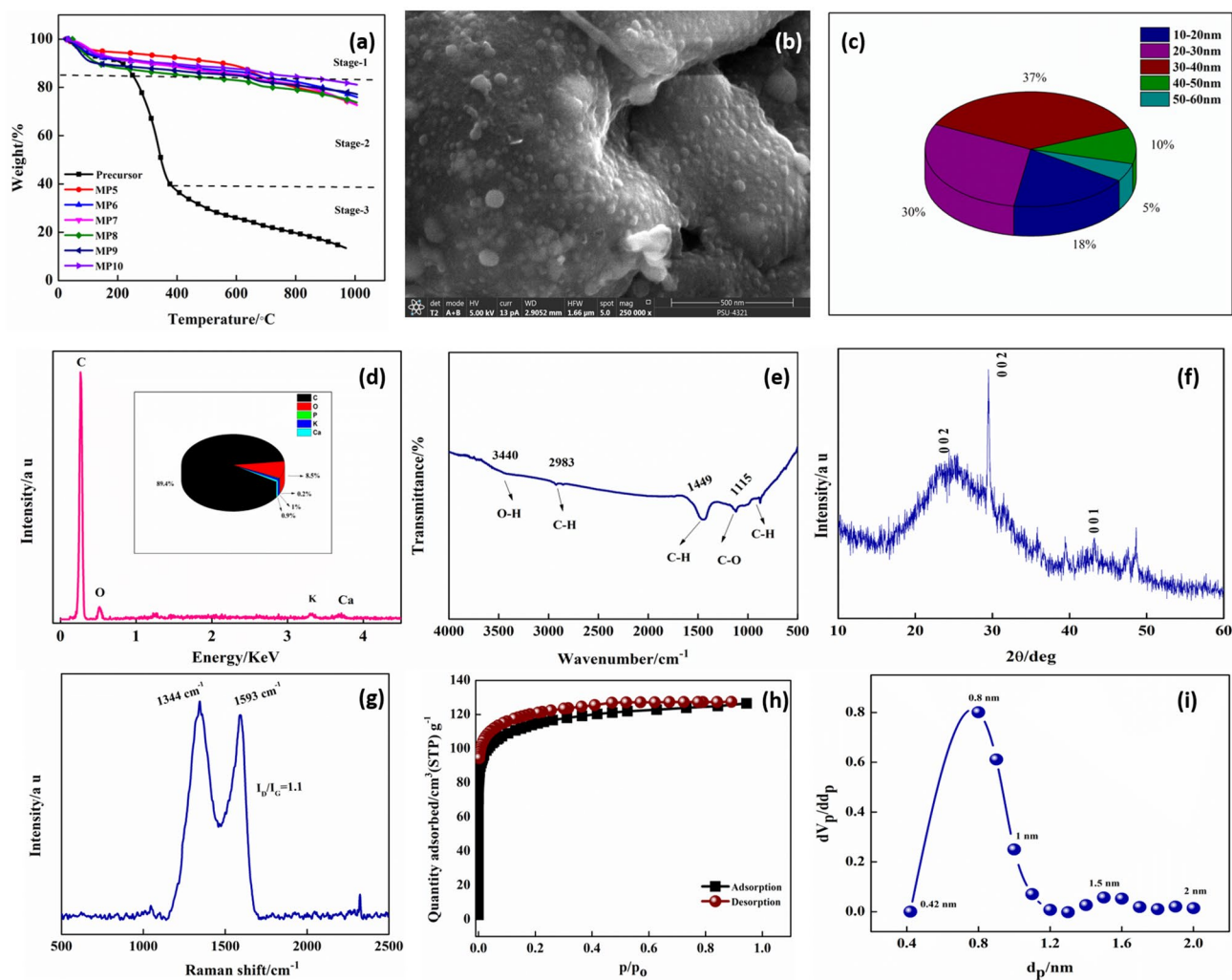


**Fig. 1** a TGA plot of precursor and MP carbon nanoparticles, b SEM image of MP10, c histogram representing carbon nanoparticles size distributions of MP10, d EDS plot of MP10; the pie chart in the inset

shows the elemental composition of MP10. FTIR spectrum (e), XRD plot (f) and Raman spectrum (g) of MP10. h  $N_2$  adsorption–desorption plot of MP10, and i pore size distribution of MP10

spheres. It is clear from Fig. S1 that the carbon nanoparticles are not discrete bodies, but are present as the aggregates of spherical bodies. This augmentation can be attributed to the long reaction times and results from cooling from the pyrolysis temperature to ambient temperature [19]. The histogram (Fig. 1c) depicting particle size distribution, is constructed using Fig. 1b. This shows that the majority of the particles have size less than 40 nm. 67% of the particles were found to be in the range of 20–40 nm.

EDS plot of prepared carbon nanoparticles are depicted in Fig. S2. Figure 1d, shows the EDS plot and the inset in Fig. 1d shows the pie chart depicting the elemental composition of the MP10 carbon nanoparticles. As the pyrolysis temperature was increased, there was a steady increase of carbon percentage. Oxygen is another element, which is present in significant quantity while some alkali metal ions are also present in trace amounts. The

self-doped oxygen also has a positive effect on the capacitance through enhancing the surface wettability of carbon materials, which benefits fast ion transport into the inner pore channels and achieves satisfactory surface accessibility for electrolyte ions, boosting the electric double-layer capacitance [20, 21].

FTIR spectrum (Fig. 1e) depicts the presence of functional groups in MP10. FTIR spectra for all the other samples are given in Fig. S3. The broad peak around  $3440\text{ cm}^{-1}$  corresponds to the O–H stretching frequency. The small less intense peak around  $2983\text{ cm}^{-1}$  can be attributed to the C–H stretching. A moderately sharp peak around  $1449\text{ cm}^{-1}$  is due to the C–H bending mode while the peak corresponding to the C–O stretching mode is observed around  $1115\text{ cm}^{-1}$ . The peak corresponding to the C–H bending mode is observed around  $877\text{ cm}^{-1}$ . The XRD pattern of MP10 (Fig. 1f) is characterized by an amorphous hump,

followed by a main diffraction peak at  $2\theta = 29^\circ$ , corresponding to the 002 graphitic plane. This is the typical pattern observed for turbostratic carbons [22]. A secondary graphite plane (001) is observed around  $2\theta = 44^\circ$ . Similar XRD patterns were observed for other MP samples (Fig. S4). In addition to XRD, Raman spectroscopy (Fig. 1g) gives more useful information regarding the carbon structural order. The two main peaks around  $1344$  and  $1593\text{ cm}^{-1}$  are commonly denoted as D-band and G-band, respectively. The diagnostic disorder in the carbon structure is indicated by the D band while the G-band represents the  $E_{2g}$  mode of vibration of  $sp^2$  bonded carbon. The relative intensities of D and G-bands ( $I_D/I_G$ ) are generally used to assess the graphitic nature of the material [19]. The  $I_D/I_G$  value for MP was found to be 1.06, indicating the presence of a greater number of edge defects in the carbon material. The Raman spectra of other MP samples are shown in Fig. S5.

Porous nature of the prepared nanomaterials was understood from the  $N_2$  adsorption–desorption isotherms. MP10 exhibited type IV isotherm (Fig. 1h) with a hysteresis loop, confirming its mesoporous nature. The  $N_2$  adsorption–desorption isotherms for other samples are shown in Fig. S6. As shown in Fig. S6, up to MP8, there is low  $N_2$  uptake. In contrast, MP9 (Fig. S6) and MP10 show a significant increase in  $N_2$  uptake along with capillary condensation at  $p/p_0 < 0.1$ , which can be ascribed to the adsorption of  $N_2$  in micropores. Porosity values of MP carbon nanoparticles obtained from  $N_2$  adsorption–desorption isotherms are tabulated in Table S1. The Brunauer–Emmett–Teller (BET) specific surface area of MP10 was found to be  $440.7\text{ m}^2\text{ g}^{-1}$ . The micropores present in MP10 contribute to the increase in the surface area of the materials. Barrett–Joyner–Halenda (BJH) method was employed to calculate the pore size distributions (Fig. 1i) Mean pore diameter was found to be 1.9 nm while the diameter of the supermicropore was 0.8 nm. The micropore volume was calculated to be  $0.20\text{ cm}^3\text{ g}^{-1}$  and the total pore volume was  $0.21\text{ cm}^3\text{ g}^{-1}$ . This indicates that the bulk of the  $N_2$  adsorption has taken place in the micropores. Much of the surface area of the material is found in the narrow micropores, also called supermicropores ( $0.7 < d < 2\text{ nm}$ ). Such type of bimodal porous structure is beneficial for electrochemical applications.

### 3.3 Electrochemical measurements

The electrochemical property of MP electrodes was investigated in 4.0 M KOH aqueous electrolyte by three-electrode configuration. Alkaline electrolytes such as KOH are cost-effective and easy to handle. KOH was chosen as the electrolyte due to its high ionic conductivity ( $\sim 0.6\text{ S cm}^{-1}$ ) at high concentrations. Figure 2 presents the cyclic voltammetry (CV) curves. CV was performed in the potential window

of  $-1.0\text{ V}$  to  $0\text{ V}$  at different scan rates ranging from 5 to  $100\text{ mV s}^{-1}$ . The rectangular CV profile at lower scan rates was only slightly deformed and showed a quasi-rectangular profile, providing evidence for well-developed capacitive behaviour. The absence of any redox peaks proves the EDLC nature of the material in KOH electrolyte.

The EDLC behavior of MP carbon electrodes was further investigated using galvanostatic charge–discharge profiles (Fig. 3) in 4.0 M KOH. The curves were linearly symmetric and triangularly shaped, which confirms the EDLC behavior of the material. Generally, the micro- and mesoporous surfaces impart high surface area, which will enhance diffusion of electrolyte thereby increasing specific capacitance and energy density of the supercapacitor [14]. The galvanostatic charge–discharge curves were measured at current densities from 0.1 to  $5.0\text{ A g}^{-1}$ . Specific capacitance was calculated using the preformulated equations reported in earlier works [14, 21]. Specific capacitance was increased at lower discharging rate (low current density) as the ions in the electrolyte solution will diffuse through entire micro and mesopores. At high charging rates the electrolyte can access only the larger pores which will diminish the specific capacitance. Variation of specific capacitance of all the MP samples, with current density is shown in Fig. 3h. Of all the samples tested, MP10 exhibited a high specific capacitance of  $356.1\text{ F g}^{-1}$  at  $0.1\text{ A g}^{-1}$ . This can be attributed to the presence of optimum bimodal pores. Also, the  $N_2$  sorption studies have indicated the presence of hierarchical micropores and mesopores. Furthermore, the presence of oxygen heteroatom also has a positive effect on the capacitance through enhancing the surface wettability of carbon materials, which benefits faster ion transportation into the inner pore channels and achieves satisfactory surface accessibility for electrolyte ions, boosting the electric double-layer capacitance [20, 21].

Electrochemical impedance spectroscopy (EIS), was performed to study the ion and electron transport behaviour at open circuit potential [21]. Figure 4a shows the Nyquist impedance plots measured in the frequency range of 0.01 to  $10^5\text{ Hz}$ . The plot depicts the typical features of porous carbon electrodes with a  $-45^\circ$  Warburg region at lower frequency and a small approximate semicircle in the high frequency region.  $R_s$  values in the range of  $1.2$ – $0.07\ \Omega$  were obtained, with  $1.2$  and  $0.07\ \Omega$  for MP5 and MP10, respectively, indicating a very low resistance at high frequency region as the pyrolysis temperature was increased. Double layer charge storage and absence of Faradic charge storage along with dependence of phase angle with frequency is also indicated by Bode plot (Fig. 4b). From the Bode plot, it is clear that MP10 in 4.0 M KOH with a phase angle of  $-84.1^\circ$  is very close to that of an ideal capacitor ( $-90^\circ$ ) [23]. Capacitances derived from the EIS test are based on the equations involving the real and imaginary part of the complex impedance, reported in earlier works [24]. Dependence

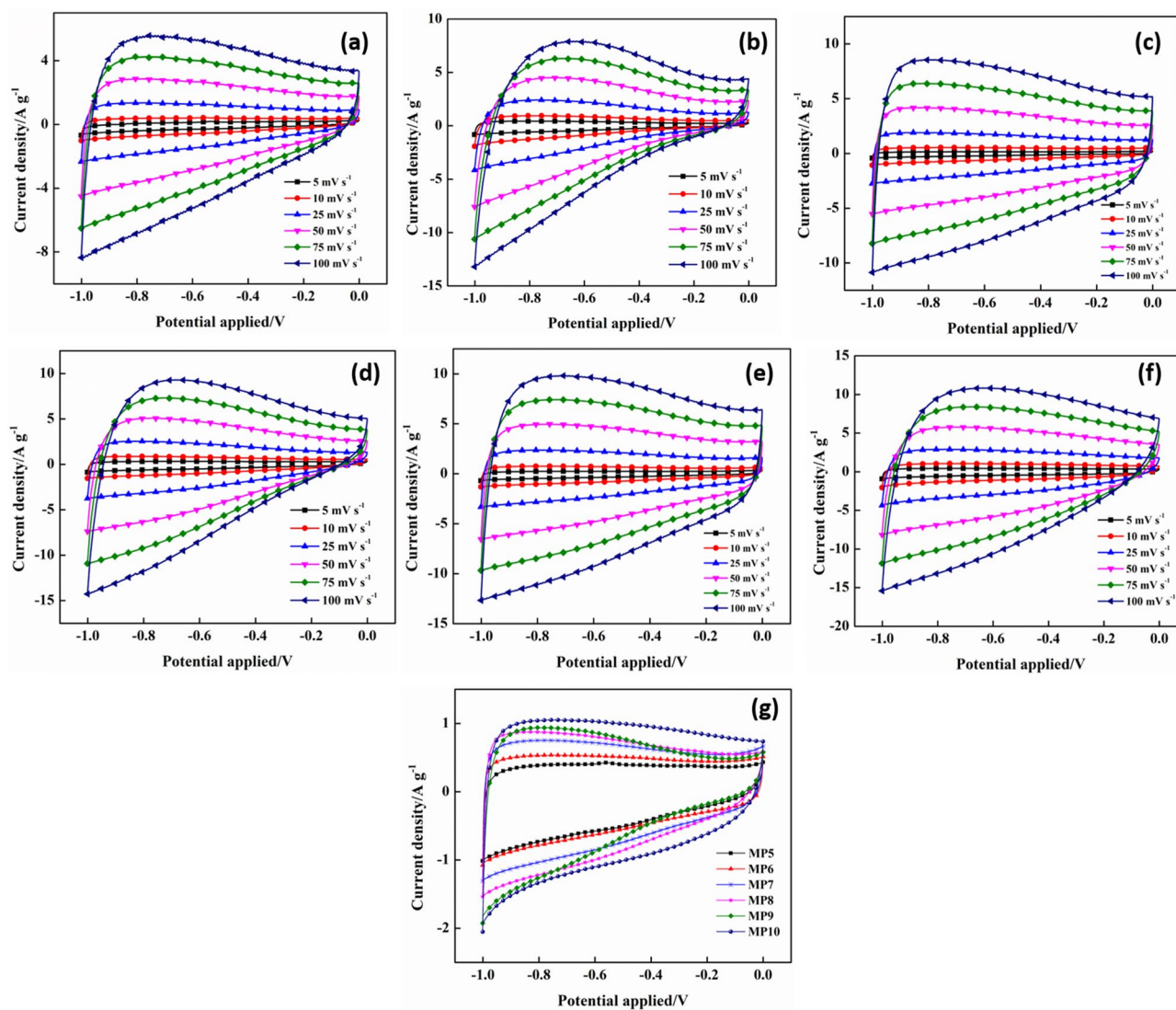


**Fig. 2** Cyclic voltammetric curves of MP5 (a), MP6 (b), MP7 (c), MP8 (d), MP9 (e), and MP10 (f) in 4.0 M KOH at different scan rates. Comparison of all the MP materials at 10 mV s<sup>-1</sup> in 4.0 M KOH (g)

of real and imaginary capacitances over frequency for all the MP samples is depicted in Fig. 4c and d respectively. For fabricating devices, it is ideal for the capacitance to remain constant with frequency after the transition between resistive and capacitive behaviours, which is appropriately represented in Fig. 4c [25]. From the plot, it is clear that only MP10 shows such ideal behaviour while for materials synthesized below 1000 °C, the capacitance continues to increase with decreasing frequency. Figure 4d depicts the imaginary part of capacitance as a function of frequency for all the MP samples. The peak of the curve is roughly considered to be a point from which the circuit changes from purely resistive to purely capacitive. The inverse of the frequency at which this transition takes place provides a parameter known as relaxation time constant ( $\tau_0$ ), which

is an indicator of the responsiveness of the supercapacitors [26]. The time constant is found to decrease with pyrolysis temperature.  $\tau_0$  for MP5 was calculated to be 5.6 s while for MP10 it was 0.25 s. This is an indication of how quickly the supercapacitor can undergo charge–discharge transitions. The  $\tau_0$  values obtained are much lower than some of those reported in earlier works on biomass derived carbons. The key parameters obtained after fitting the data are tabulated in Table 1.

### 3.4 Practical symmetrical supercapacitor

CR2032 coin cell, a symmetrical supercapacitor, was made using MP10, as it showed a high specific capacitance (356.1 F g<sup>-1</sup>). Figure 5a shows the CV plot with

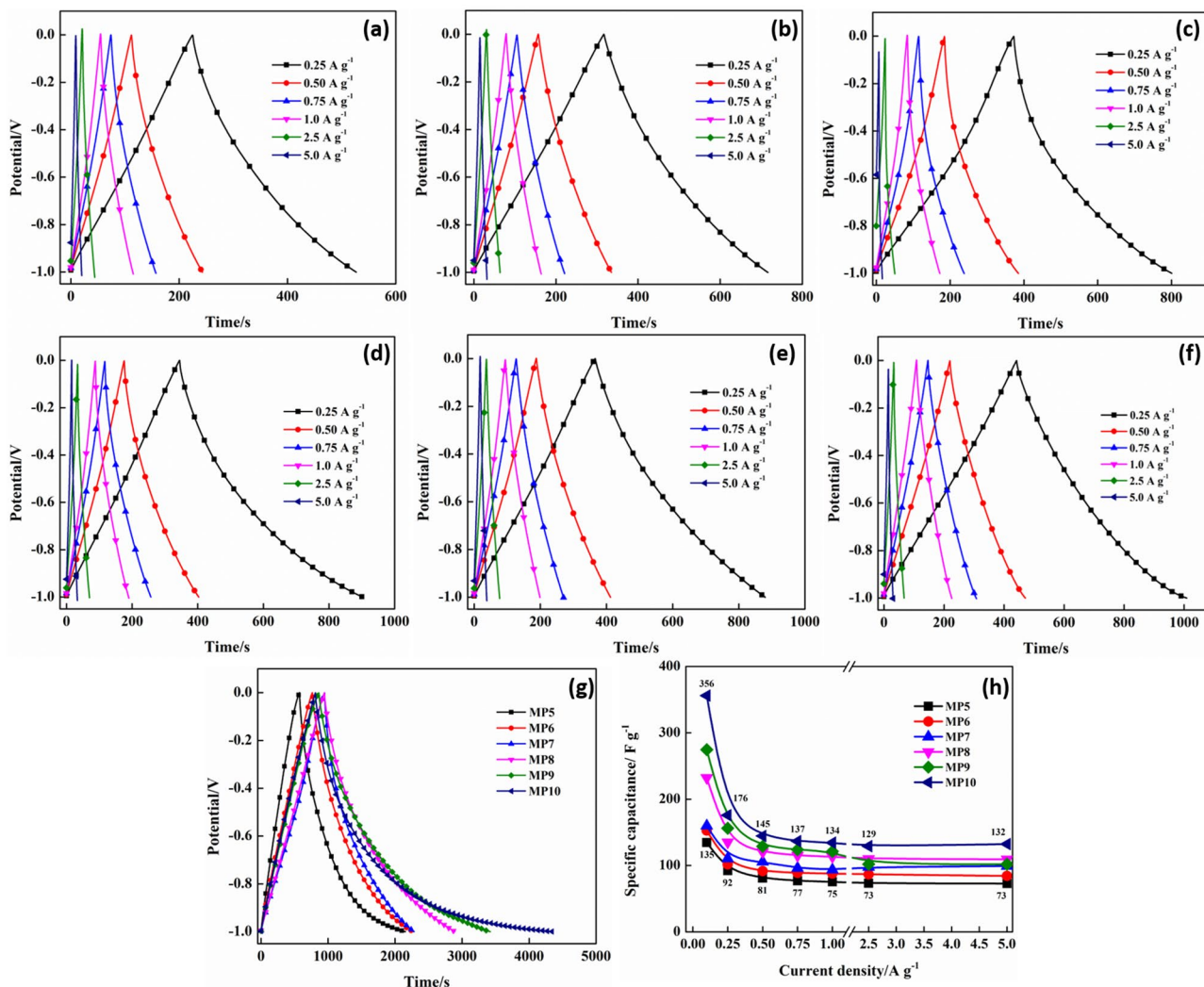


**Fig. 3** Galvanostatic charge–discharge curves of MP5 (a), MP6 (b), MP7 (c), MP8 (d), MP9 (e), and MP10 (f) in 4.0 M KOH at different current densities. Comparison of all the MP materials at 0.1 A g<sup>-1</sup> in 4.0 M KOH (g). Plot of variation of specific capacitance with current density (h)

1.0 V cell voltage. At lower scan rate (10 mV s<sup>-1</sup>), the CV can be seen with slight rounded top left and bottom right corners of the rectangular curve. The loss of rectangular shapes was seen with an increase in scan rate. However, the absence of any characteristic redox peaks when the cell voltage was increased from 1.0 to 1.5 V (Fig. 5b) indicates capacitive behaviour and signifies the capability of MP10 device for operating at higher potential windows. Overpotential was observed when the applied potential was increased above 1.5 V. Hence, charge–discharge studies were restricted to 1.4 V. Charge–discharge curves at different current densities from 0.1 to 2.5 A g<sup>-1</sup> under 1.0 V (Fig. 5c) displayed a triangular, linear and symmetrical nature without any significant IR drop, confirming the EDLC behaviour and good electrochemical reversibility of the MP10 cell. Figure 5d depicts retention of triangular nature of the galvanostatic

charge–discharge curves at different potential windows. Variation of specific capacitance with current density is depicted in Fig. 5e. In the three electrode setup, a complete potential window is applied on the working electrode wherein for a symmetrical supercapacitor device/cell, the applied voltage is shared between the two electrodes [27]. For the same reason, the capacitances are lower than that obtained for MP10 in three electrodes set up (356.1 F g<sup>-1</sup>). The fabricated supercapacitor cell had a C<sub>sp</sub> of, 126.8 F g<sup>-1</sup>, 124.8 F g<sup>-1</sup> and 124.6 F g<sup>-1</sup> at 1.4, 1.2 and 1.0 V operating potential at 0.1 A g<sup>-1</sup>. The key energy performance is listed in Table 2. Impedance of the cell as a function of frequency was done by EIS testing. The Nyquist plot shows a semicircle in the high frequency region and a linear line in the low frequency region (Fig. 5f). The plot indicates presence of surface impedance, ion transfer resistance and Warburg

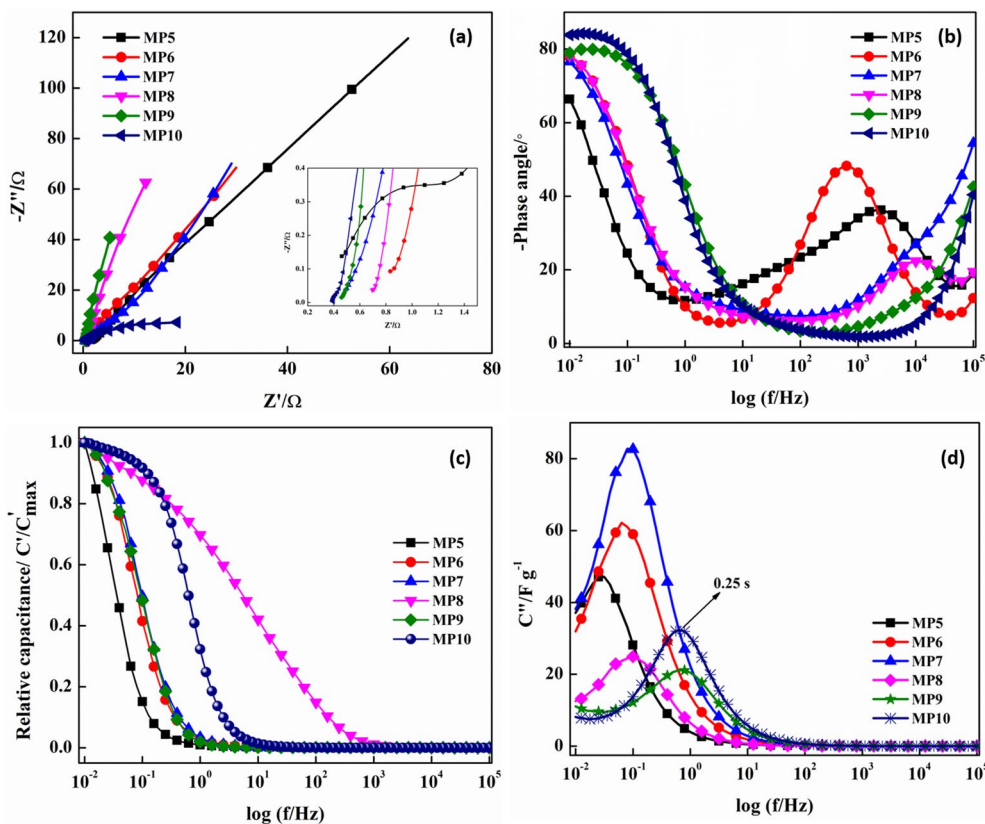


**Fig. 4** **a** Nyquist impedance plot of MP5, MP6, MP7, MP8, MP9 and MP10 in 4.0 M KOH. The inset shows the high frequency region of the Nyquist plot. **b** Plot of Bode phase angle as a function of fre-

quency and **c** and **d** are the real and imaginary capacitance as a function of frequency respectively

impedance. The Bode plot (Fig. 5g) was used to demonstrate cell response between the phase angle and the

**Table 1** Fitted key parameters of electrochemical impedance measurements

Material	$R_S$ ( $\Omega$ )	$R_{CT}$ ( $\Omega$ )	C (mF)	CPE (F)	W ( $\Omega$ )
MP5	1.2	4.9	0.234	0.225	0.263
MP6	0.5	0.9	0.021	0.862	0.422
MP7	0.4	0.5	0.32	0.047	0.425
MP8	0.3	0.6	0.038	0.262	0.863
MP9	0.5	0.3	0.26	0.0004	0.529
MP10	0.07	0.2	0.050	0.38	1.456
MP10Cell <sup>a</sup>	3.9	3.6	0.0067	0.053	0.053
MP10Cell <sup>b</sup>	5.4	13.7	0.000264	0.00279	0.07

<sup>a</sup>Before 10,000 charge–discharge cycles

<sup>b</sup>After 10,000 charge–discharge cycles

frequency. The real and imaginary parts of the capacitances calculated are depicted in Fig. 5h as a function of frequency.  $\tau_0$  for the MP10 device was found to be

4.8 s. The equivalent circuit model was used to fit the experimental data and to derive the EIS parameters. The obtained values are listed in Table 1.

The energy and power densities of the symmetric cell, were calculated using the following equations [28]:

$$E \text{ (Wh kg}^{-1}\text{)} = \frac{C_{sp} \times (V_{max}^2 - V_{min}^2)}{7.2}, \quad (2)$$

$$P \text{ (W kg}^{-1}\text{)} = \frac{Ex3600}{t}, \quad (3)$$

where  $C_{sp}$  ( $F g^{-1}$ ) is the specific capacitance calculated from charge–discharge cycles,  $\Delta V$  (V) is the voltage and  $t$  (s) is the discharge time during the galvanostatic charge–discharge measurements. Ragone plot depicting variation of energy density with power density is shown in Fig. 6a. A very high energy density of  $34.5 \text{ Wh kg}^{-1}$  is reached at a power density of  $494.5 \text{ W kg}^{-1}$  at 1.4 V. The energy and power densities were inversely related; that is, as power density increases, energy density decreases. At a very high-power density of  $12.2 \text{ kW kg}^{-1}$ , energy density could still be retained at  $18.5 \text{ Wh kg}^{-1}$ . The obtained values are much



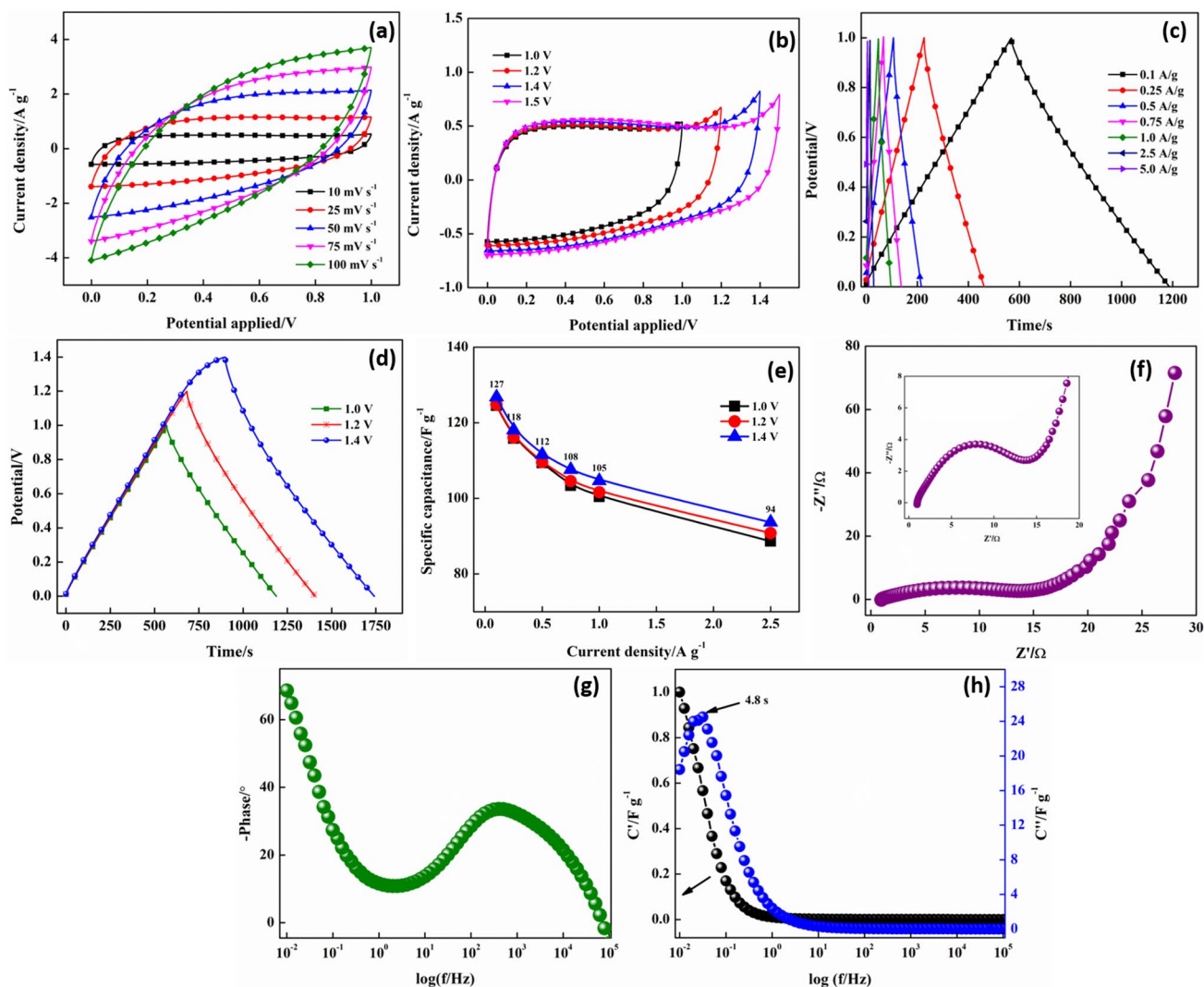


**Fig. 5** **a** CV of MP10 symmetric cell at different scan rates in 4.0 M KOH. **b** CV at  $10 \text{ mV s}^{-1}$  under different potential windows. **c** Galvanostatic charge–discharge curves at different current densities. **d** Galvanostatic charge–discharge curves under different potential windows at  $0.1 \text{ A g}^{-1}$ . **e** Specific capacitance of the cell as a function of current

density. **f** Nyquist impedance plot of the cell at OCP. The inset shows the high frequency region. **g** Bode phase angle plot as a function of frequency and **h** real and imaginary parts of the capacitances derived from impedance studies

**Table 2** Key energy performance parameters of MP10 symmetric supercapacitor

Symmetric coin cell device	Potential (V)	Current density (A g <sup>-1</sup> )	Specific capacitance (F g <sup>-1</sup> )	Energy density (Wh kg <sup>-1</sup> )	Power density (W kg <sup>-1</sup> )
MP10	1.0	0.1	124.6	17.3	73.9
		2.5	88.7	7.8	2003.2
	1.2	0.1	124.8	25	124.3
		2.5	90.8	11.3	3400.6
	1.4	0.1	126.8	34.5	494.5
		2.5	93.7	18.5	12,215.8

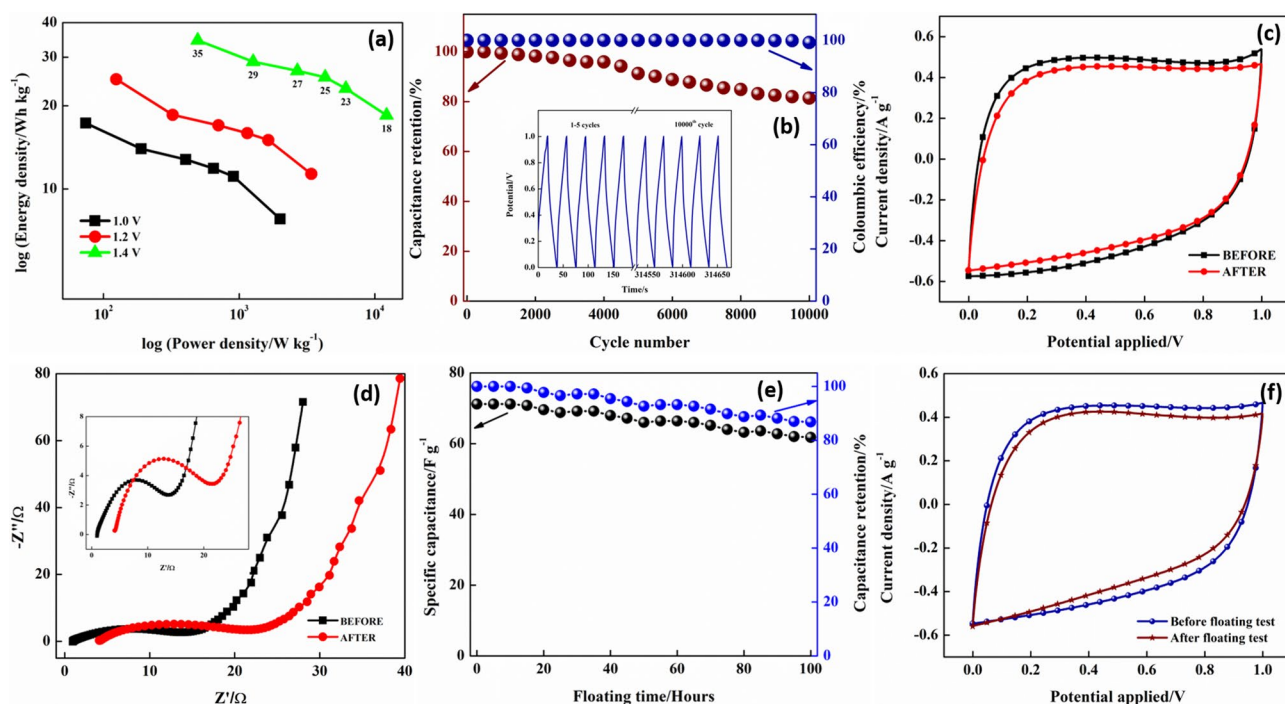


**Fig. 6** **a** Ragone plot of MP10 symmetric cell, **b** capacitance retention and Coulombic efficiency as function of charge–discharge cycle number. The inset shows the initial and final charge–discharge curves at  $2.0 \text{ A g}^{-1}$  during 10,000 cycles. **c** CV depicting efficiency of the device before and after 10,000 cycles at  $10 \text{ mV s}^{-1}$ . **d** Nyquist imped-

ance plot depicting an increase of impedance after 10,000 cycles. **e** Floating test indicating capacitance retention over 100 h at  $2.0 \text{ A g}^{-1}$ . **f** CV depicting the changes in the electrochemical nature of the device before and after the floating test

higher than some of those reported in recent works [29–32]. The energy and power density values calculated at different current densities and operating potentials are given in Table 2. Cycling stability is an essential factor for supercapacitor electrodes. Stability studies were performed using galvanostatic charge–discharge cycling at a current density of  $2.0 \text{ A g}^{-1}$  for 10,000 cycles, as shown in Fig. 6b. The symmetric cell exhibited 81.4% capacitance retention at the end of 10,000th charge/discharge cycle (Fig. 6b), indicating excellent cycling ability. The cell also exhibited seamless

Coulombic efficiency of 99.2% even after 10,000 cycles which could be attributed to effective accessibility for the ions onto the porous surface of electrode. The stability of the device was also tested by floating method (aging), as shown in Fig. 6e, which shows the voltage-holding curve at  $2.0 \text{ A g}^{-1}$  for a period of 100 h, which showed 86.8% capacitance retention throughout the aging time, signifying that the cell exhibited remarkable stability throughout.

A red LED bulb was connected to a single MP10 coin cell, which glowed for 3.4 min on charging for 20 s

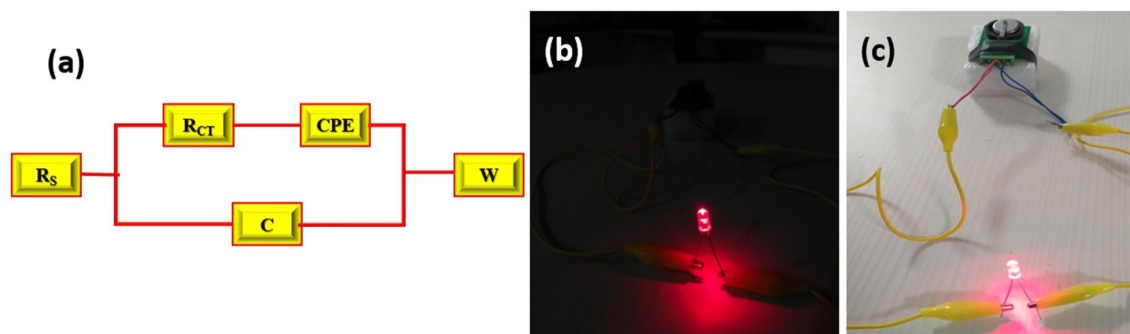


**Fig. 7** **a** Equivalent circuit of MP10 coin cell obtained from impedance data, red LED glow in dark **(b)** and bright **(c)** conditions using MP10 coin cell. (Color figure online)

**Table 3** Performance comparison of various biomass derived carbon used in device setups with this work

Precursor	Voltage (V)	Capacitance (F g <sup>-1</sup> )	Scan rate	Electrolyte	Energy density (Wh kg <sup>-1</sup> )	References
Milk protein–SDS–graphene	1.6	120.8	0.1	LiSO <sub>4</sub>	36.7	[36]
<i>Typha angustifolia</i>	0.8	–	5 mV s <sup>-1</sup>	0.5 M K <sub>2</sub> SO <sub>4</sub>	19.0	[37]
Activated carbon/MnO <sub>2</sub>	1.8	27.3	1 mV s <sup>-1</sup>	1M Na <sub>2</sub> SO <sub>4</sub>	9.4	[38]
Bamboo	3.5	146	0.2 A g <sup>-1</sup>	EMIMTFSI	6.1	[39]
Rubber wood	1.0	138	0.01 A cm <sup>-2</sup>	H <sub>2</sub> SO <sub>4</sub>	2.63	[40]
Elm seeds	2.0	23.3	1.0 A g <sup>-1</sup>	KOH	18.6	[41]
Cashew nut husk	1.0	121	0.5 A g <sup>-1</sup>	1 M Na <sub>2</sub> SO <sub>4</sub>	11.2	[42]
Pine cone	1.6	69	0.5 A g <sup>-1</sup>	Gel electrolyte	24.6	[43]
<b><i>Touch-me-not leaves</i></b>	<b>1.4</b>	<b>126.8</b>	<b>0.1 A g<sup>-1</sup></b>	<b>4 M KOH</b>	<b>34.5</b>	<b>This work</b>

Bold signifies the current work

(Fig. 7). This indicates that the synthesized carbon materials have a huge capacity for a high-performance electrode in electrochemical storage applications. The obtained energy parameters were compared with those reported in some of the previously published works on porous carbons for energy storage applications (Table 3). The comparison highlights the availability of high energy density of the MP10 material.

## 4 Conclusions

Biomass precursors possess a novel inherent structure and composition. Optimized pyrolysis technique can be used to prepare sustainable, high capacitive carbon with sufficient surface area and interconnected bimodal porous structures. Since the precursor used here is abundantly available and for preparation, a single step is followed without using any activating agents, the method is cost effective. The present work demonstrated the use of such abundant biomass as raw material for the synthesis of porous carbon nanomaterials with good electrochemical properties. Reaching high energy density of 34.5 Wh kg<sup>-1</sup> at 494.5 W kg<sup>-1</sup> could prove beneficial for application in hybrid energy storage systems [33–35] with cell assembly. MP10 carbon nanoparticle is boon to clean technology which can complement and reduce excess load on batteries thereby lessening the burden on the environment. The tuning of MP materials is in progress with respect to different electrolyte concentrations, functionalizing the MP, activating the carbon materials and will be reported elsewhere.

**Acknowledgements** Dr. Gurumurthy Hegde acknowledges DST-Nano-mission, Government of India, for funding the Project ‘Biomass based porous nano materials for efficient low-cost energy storage devices’

with Grant No. SR/NM/NT-1026/2017. We would like to thank Supriya S. for the initial synthesis of presented materials. We also thank Dr. Mahaveer Kurkure and Mr. Ganesan Sriram for helping in BET measurements. We would like to thank Dr. Thitima Rujiralai and Dr. Titilope for SEM and Raman measurements.

## Compliance with ethical standards

**Conflict of interest** The authors declare that there is no conflict of interest.

## References

- Simon P, Gogotsi Y, Dunn B (2014) Where do batteries end supercapacitors begin? *Science* 343(6176):1210–1211
- Ma H, Chen Z, Gao X, Liu W, Zhu H (2019) 3D hierarchically gold-nanoparticle-decorated porous carbon for high-performance supercapacitors. *Sci Rep* 9(1):17065
- Hegde G, Iyer D (2015) Activated carbon nanospheres derived from bio-waste materials for supercapacitor applications—a review. *RSC Adv* 5(107):88339–88352
- Chmiola J, Yushin G, Gogotsi Y, Portet C, Simon P, Taberna PL (2006) Anomalous increase in carbon capacitance at pore sizes less than 1 nanometer. *Science* 313(5794):1760
- Zhang Y, Chen H, Wang S, Zhao X, Kong F (2020) Regulatory pore structure of biomass-based carbon for supercapacitor applications. *Microporous Mesoporous Mater* 297:110032
- Akshaya KB, Bhat VS, Varghese A, George L, Hegde G (2019) Non-enzymatic electrochemical determination of progesterone using carbon nanospheres from onion peels coated on carbon fiber paper. *J Electrochem Soc* 166(13):B1097–B1106
- Wang J, Zhang X, Li Z, Ma Y, Ma L (2020) Recent progress of biomass-derived carbon materials for supercapacitors. *J Power Sources* 451:227794
- Gong Y, Li D, Fu Q, Zhang Y, Pan C (2020) Nitrogen self-doped porous carbon for high-performance supercapacitors. *ACS Appl Energy Mater* 3(2):1585–1592
- Lu Q, Zhou S, Li B, Wei H, Zhang D, Hu J, Zhang L, Zhang J, Liu Q (2020) Mesopore-rich carbon flakes derived from lotus leaves

- and its ultrahigh performance for supercapacitors. *Electrochim Acta* 333:135481
10. Li Y, Zhang D, Zhang Y, He J, Wang Y, Wang K, Xu Y, Li H, Wang Y (2020) Biomass-derived microporous carbon with large micropore size for high-performance supercapacitors. *J Power Sources* 448:227396
  11. Ji L, Wang B, Yu Y, Wang N, Zhao J (2020) S co-doped biomass derived carbon with sheet-like microstructures for supercapacitors. *Electrochim Acta* 331:135348
  12. Zhang X, Zhang Z, Zhou Z (2018) MXene-based materials for electrochemical energy storage. *J Energy Chem* 27(1):73–85
  13. Xu H, Wang Y, Liao X, Shi B (2020) A collagen-based electrolyte-locked separator enables capacitor to have high safety and ionic conductivity. *J Energy Chem* 47:324–332
  14. Ali GAM, Manaf SAA, Divyashree A, Chong KF, Hegde G (2016) Superior supercapacitive performance in porous nanocarbons. *J Energy Chem* 25(4):734–739
  15. Ali GAM, Manaf SABA, Kumar A, Chong KF, Hegde G (2014) High performance supercapacitor using catalysis free porous carbon nanoparticles. *J Phys D* 47(49):495307
  16. Hegde G, Abdul Manaf SA, Kumar A, Ali GAM, Chong KF, Ngaini Z, Sharma KV (2015) Biowaste Sago bark based catalyst free carbon nanospheres: waste to wealth approach. *ACS Sustain Chem Eng* 3(9):2247–2253
  17. Kumar A, Hegde G, Manaf SABA, Ngaini Z, Sharma KV (2014) Catalyst free silica templated porous carbon nanoparticles from bio-waste materials. *Chem Commun* 50(84):12702–12705
  18. Yang H, Yan R, Chen H, Zheng C, Lee DH, Liang DT (2006) In-depth investigation of biomass pyrolysis based on three major components: hemicellulose, cellulose and lignin. *Energy Fuels* 20(1):388–393
  19. Nieto-Márquez A, Romero R, Romero A, Valverde JL (2011) Carbon nanospheres: synthesis, physicochemical properties and applications. *J Mater Chem* 21(6):1664–1672
  20. Feng W, He P, Ding S, Zhang G, He M, Dong F, Wen J, Du L, Liu M (2016) Oxygen-doped activated carbons derived from three kinds of biomass: preparation, characterization and performance as electrode materials for supercapacitors. *RSC Adv* 6(7):5949–5956
  21. Ali GAM, Supriya S, Chong KF, Shaaban ER, Algarni H, Maiyalagan T, Hegde G (2019) Superior supercapacitance behavior of oxygen self-doped carbon nanospheres: a conversion of *Allium cepa* peel to energy storage system. *Biomass Convers Biorefin*. <https://doi.org/10.1007/s13399-019-00520-3>
  22. Supriya S, Sriram G, Ngaini Z, Kavitha C, Kurkuri M, De Padova IP, Hegde G (2019) The role of temperature on physical–chemical properties of green synthesized porous carbon nanoparticles. *Waste Biomass Valoriz*. <https://doi.org/10.1007/s12649-019-00675-0>
  23. Ali GAM, Divyashree A, Supriya S, Chong KF, Ethiraj AS, Reddy MV, Algarni H, Hegde G (2017) Carbon nanospheres derived from *Lablab purpureus* for high performance supercapacitor electrodes: a green approach. *Dalton Trans* 46(40):14034–14044
  24. Zhang S, Pan N (2015) Supercapacitors performance evaluation. *Adv Energy Mater* 5(6):1401401
  25. Largeot C, Portet C, Chmiola J, Taberna P-L, Gogotsi Y, Simon P (2008) Relation between the ion size and pore size for an electric double-layer capacitor. *J Am Chem Soc* 130(9):2730–2731
  26. Gogotsi Y, Simon P (2011) True performance metrics in electrochemical energy storage. *Science* 334(6058):917–918
  27. Li Z, Zhang L, Amirkhiz BS, Tan X, Xu Z, Wang H, Olsen BC, Holt CMB, Mitlin D (2012) Carbonized chicken eggshell membranes with 3D architectures as high-performance electrode materials for supercapacitors. *Adv Energy Mater* 2(4):431–437
  28. Zequine C, Ranaweera CK, Wang Z, Singh S, Tripathi P, Srivastava ON, Gupta BK, Ramasamy K, Kahol PK, Dvornic PR, Gupta RK (2016) High performance and flexible supercapacitors based on carbonized bamboo fibers for wide temperature applications. *Sci Rep* 6:31704
  29. Misnon II, Zain NKM, Lei TS, Vijayan BL, Jose R (2020) Activated carbon with graphitic content from stinky bean seedpod bio-waste as supercapacitive electrode material. *Ionics* 26:4089–4093
  30. Jiang X, Guo F, Jia X, Liang S, Peng K, Qian L (2020) Synthesis of biomass-based porous graphitic carbon combining chemical treatment and hydrothermal carbonization as promising electrode materials for supercapacitors. *Ionics* 26:3655–3668
  31. Wan L, Hu S, Liu J, Chen D, Liu S, Xiao R, Zhang Y, Chen J, Du C, Xie M (2020) Enhancing the energy density of supercapacitors by introducing nitrogen species into hierarchical porous carbon derived from camellia pollen. *Ionics* 26:2549–2561
  32. Ishita I, Singhal R (2020) Porous multi-channel carbon nanofiber electrodes using discarded polystyrene foam as sacrificial material for high-performance supercapacitors. *J Appl Electrochem* 50:809–820
  33. Ciccarelli F, Iannuzzi D, Tricoli P (2012) Control of metro-trains equipped with onboard supercapacitors for energy saving and reduction of power peak demand. *Transp Res C* 24:36–49
  34. Khosrozadeh A, Xing M, Wang Q (2015) A high-capacitance solid-state supercapacitor based on free-standing film of polyaniline and carbon particles. *Appl Energy* 153:87–93
  35. Wang Y, Sun Z, Chen Z (2019) Energy management strategy for battery/supercapacitor/fuel cell hybrid source vehicles based on finite state machine. *Appl Energy* 254:113707
  36. Chen H, Lu X, Wang H, Sui D, Meng F, Qi W (2020) Controllable fabrication of nitrogen-doped porous nanocarbons for high-performance supercapacitors via supramolecular modulation strategy. *J Energy Chem* 49:348–357
  37. Liu W-J, Tian K, Ling LL, Yu H-Q, Jiang H (2016) Use of nutrient rich hydrophytes to create N, P-dually doped porous carbon with robust energy storage performance. *Environ Sci Technol* 50(22):12421–12428
  38. Liu H, Zhao K (2016) Asymmetric flow electrochemical capacitor with high energy densities based on birnessite-type manganese oxide nanosheets and activated carbon slurries. *J Mater Sci* 51(20):9306–9313
  39. Kim YJ, Horie Y, Ozaki S, Matsuzawa Y, Suezaki H, Kim C, Miyashita N, Endo M (2004) Correlation between the pore and solvated ion size on capacitance uptake of PVDC-based carbons. *Carbon* 42(8):1491–1500
  40. Taer E, Deraman M, Talib I, Awitdrus A, Hashmi S, Umar A (2011) Preparation of a highly porous binderless activated carbon monolith from rubber wood sawdust by a multi-step activation process for application in supercapacitors. *Int J Electrochem Sci* 6(8):3301–3315
  41. Guo D, Song X, Li B, Tan L, Ma H, Pang H, Wang X, Zhang L, Chu D (2019) Oxygen enriched carbon with hierarchical porous structure derived from biomass waste for high-performance symmetric supercapacitor with decent specific capacity. *J Electroanal Chem* 855:113349
  42. Cai N, Cheng H, Jin H, Liu H, Zhang P, Wang M (2020) Porous carbon derived from cashew nut husk biomass waste for high-performance supercapacitors. *J Electroanal Chem* 861:113933
  43. Barzegar F, Bello A, Dangbegnon JK, Manyala N, Xia X (2017) Asymmetric supercapacitor based on activated expanded graphite and pine cone tree activated carbon with excellent stability. *Appl Energy* 207:417–426

**Publisher's Note** Springer Nature remains neutral with regard to jurisdictional claims in published maps and institutional affiliations.

## Affiliations

Vinay S. Bhat<sup>1,2</sup> · Gurumurthy Hegde<sup>1</sup> · Mahmoud Nasrollahzadeh<sup>3</sup>

✉ Gurumurthy Hegde  
murthyhegde@gmail.com

✉ Mahmoud Nasrollahzadeh  
mahmoudnasr81@gmail.com

<sup>2</sup> Department of Materials Science, Mangalore University,  
Mangalagangotri, Mangalore, Karnataka 574199, India

<sup>3</sup> Department of Chemistry, Faculty of Science, University  
of Qom, Qom 3716146611, Iran

<sup>1</sup> Centre for Nano-Materials & Displays (CND), B.M.S.  
College of Engineering, Bangalore, Karnataka 560019, India